Light Field Convergency: Implicit Photometric Consistency on Transparent Surface

Yuta Ideguchi, Yuki Uranishi, Shunsuke Yoshimoto, Yoshihiro Kuroda and Osamu Oshiro[1]
Osaka University, 1–3 Machikaneyama, Toyonaka, Osaka, 560–8531 Japan
y-ideguchi@cj.jp.nec.com

Abstract

This paper proposes a method for estimating the surface of transparent objects based on light field convergency. The light field convergency represents the degree of convergence of the light field at each point. The proposed method utilizes local photo consistency, which is one of characteristics of the light field convergency. Around a boundary contour, a point that is visible from viewpoints with a small convergence angle is locally consistent. In other words, the local photo consistency is implicitly maintained near the boundary contour. We use a light field camera as a camera array with small convergence angles to estimate the surface of the transparent object. Experimental results have demonstrated that the depth of the transparent object is estimated from the captured image by the light field camera.

1. Introduction

Although several methods have been proposed for measuring the shape of an object which has a non-Lambertian surface, surface shape measurement of transparent objects is still a difficult problem in the field of computer vision. For measuring the surface shape of the transparent object, several researchers have proposed methods including methods [16, 13] using polarized light and a method [7] by soaking an object in the fluorescent emission solution. However, the method using polarized light needs to surround the object with light sources for the measurement. On the other hand, the method using the fluorescent emission solution is invasive because of the necessity of immersing the object in the solution. Other approaches [22, 21] using light field have been proposed for measuring the surface shape of a thin transparent object. The approach aims at measuring the surface shape of a thin transparent object, and the approach is not applicable to measure the surface shape of a solid transparent object. However, light field has many helpful information which can be acquired all at once.

We propose a method for estimating the surface of a transparent object based on *light field convergency*. The light field convergency is a feature representing a convergence of the light field within the space. A transparent object is captured by the light field camera [15, 2, 23], and the depth and the normal direction are estimated simultaneously. The depth is estimated using local photo consistency that is one of the characteristics of light field convergency. The local photo consistency is a property which is observable around boundary contours of a transparent object. The point on the transparent object looks the same from the viewpoints which have a small convergence angle. The normal direction is estimated using a light field convergency map that describes the distribution of light field convergency. In this paper, the results show that the normal direction of surface and the depth at the boundary contour of the transparent object are estimated from the captured image by the light field camera.

The proposed method several characteristics, as follows:

- *Real-time oriented.* The proposed method can estimate the shape of a transparent object from image which were captured in one shot. The proposed method can measure the shape even if the objects deform.
- *Real-world oriented.* The proposed method does not need particular light and calibration between camera and measurement environment. Not only transparent object but also opaque object are estimated by the same framework. Specifically, it can be used as eye of working robot.
- *IOR-free* The calculation of the proposed method does not include refractive index. Additionally, a transparent object may have distribution of the refractive index.

2. Related Works

Several methods including [17, 5] have been developed to measure the three-dimensional shape of the object. Some of them have also been commercialized including Microsoft

[1]Yuta Ideguchi is currently with NEC Corporation, Japan. This work was supported by JSPS KAKENHI Grant Number 16K00272.

Kinect [1]. In such methods, it is difficult to measure the shape of the object in case that the surface is non-Lambertian such as a specular reflection, a subsurface scattering, or a transmission. Method [11] measures a three-dimensional shape of the metallic surfaces by utilizing the polarization. There are also methods [14, 10] for shape and radiance of specular surfaces. Other methods [8, 9] utilize a single scattered light to measure a translucent three-dimensional object shape.

Some methods have focused to measure the three-dimensional shape of transparent objects which cause refraction and transmission. In methods [13, 16] using polarized light, a reflected light on the surface of transparent objects is observed by a camera via a polarization plate. Polarization intensity of the reflected light varies according to the angle of reflection. Angles at each point on the surface of transparent objects are measured by observing while rotating a polarizing plate passing the polarization of certain angles. In this method, it is necessary to surround the transparent object with light sources. In a method [7] using fluorescence liquid, the transparent object immersed in fluorescence liquid is measured by irradiating a slit light. The slit light causes the fluorescent emission in the fluorescent solution.

Recently, many methods [3, 4, 20, 18, 19] employ a camera capable of recording the light field. A method [12], using a camera capable of recording the light field, identifies the transparent object from refraction of the light rays passing through the transparent object. This method identifies the transparent object by pre-registering the light field of transparent objects. However, this method is not intended to measure the surface shape of the transparent object. To measure the surface shape of the transparent object, methods [22, 21] that utilize light field have been proposed. In this method, light of the background is coded in position and angle. Position and angle of the light at background are determined by observing the light passing through the transparent object via a camera. The surface shape of the transparent object is estimated from those information by assuming the transparent object with a thin lens. Therefore, this method can not measure the surface shape of the thick transparent objects.

In this paper, we propose a novel approach for estimating position and direction, on the surface of a transparent object based on *light field convergency*. The acquired image by light field camera is regarded as the images by an array of virtual cameras. In the proposed method, it is easy to build a system because the surface shape of the transparent object is estimated using a single light field camera.

3. Local Photo Consistency

Photo-consistency is a property in which a point on the object has the same appearance from arbitrary viewpoints. For example, an observed color does not depend on the viewpoint on Lambertian surface, because the ray is diffused isotropically. On the Lambertian surface, the corresponding points are identified based on the photo-consistency, then the depth of the point can be measured with the stereo matching-based method. On the other hand, a transparent object, such as a glass product, has a property in which rays from the outside penetrates the object. Therefore, the color of the apparent varies depending on the point of view, i.e. it is not photo-consistent. For this reason, measuring the shape of the transparent object is relatively difficult.

As shown in Figure 1 (a), let us consider the refraction of ray at a transparent object.Since there is a difference between the refractive rates, a ray is refracted at a borderline between an air and the inside of the object. In this paper, it is assumed that the refractive rates of the transparent object is homogenous, and the light is not scattered inside the object. As shown in Fig. 1 (a), let θ_{air} be the inside angles, θ_{tra} denotes the outside angles, n_{air} is the refractive rates of the air, n_{tra} is the refractive rates of transparent object. These relationships are as follows according to Snell's law [6]:

$$n_{\mathrm{air}} \sin\theta_{\mathrm{air}} = n_{\mathrm{tra}} \sin\theta_{\mathrm{tra}}, \quad (1)$$

$$\theta_{\mathrm{tra}} = \sin^{-1}\left(\frac{\sin\theta_{\mathrm{air}}}{n}\right), \quad (2)$$

where $n = n_{\mathrm{tra}}/n_{\mathrm{air}}$. This equation is differentiated by θ_{air} as follows:

$$\Psi(\theta_{\mathrm{air}}) = \frac{\partial\theta_{\mathrm{tra}}}{\partial\theta_{\mathrm{air}}} = \frac{\cos\theta_{\mathrm{air}}}{\sqrt{n^2 - \sin^2\theta_{\mathrm{air}}}}. \quad (3)$$

Therefore, $\Delta\theta_{\mathrm{tra}}$ is written the following equation:

$$\begin{aligned}\Delta\theta_{\mathrm{tra}} &\approx \Psi(\theta_{\mathrm{air}})\Delta\theta_{\mathrm{air}} = \frac{\partial\theta_{\mathrm{tra}}}{\partial\theta_{\mathrm{air}}}\Delta\theta_{\mathrm{air}} \\ &\approx \frac{\cos\theta_{\mathrm{air}}}{\sqrt{n^2 - \sin^2\theta_{\mathrm{air}}}}\Delta\theta_{\mathrm{air}}. \end{aligned} \quad (4)$$

Therefore, when looking around center of the transparent object ($\theta_{\mathrm{air}} \approx 0$), $\Delta\theta_{\mathrm{tra}} = \Delta\theta_{\mathrm{air}}/n$. In the case of most of the transparent object, θ_{tra} changes with θ_{air} because $1 \leq n < 2.5$. In this way, the photo-consistency is not maintained.

On the other hand, as shown in Figure 1 (b), let us consider the refraction of ray at the boundary contour of the transparent object. In this study, a part of surface where the line of sight and the normal to the surface around that part are nearly perpendicular is regarded as boundary contour. When $\theta_{\mathrm{air}} = \pi/2$, $\Psi(\theta_{\mathrm{air}}) = 0$ from the Equation (3), so that $\Delta\theta_{\mathrm{tra}} = 0$. Expressing $\Psi(\theta_{\mathrm{air}})$ by a second-order

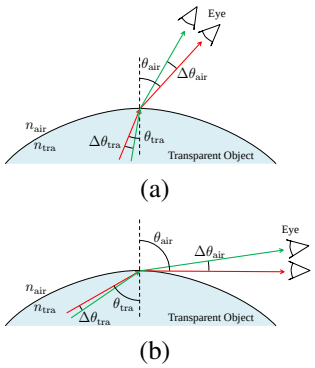

Figure 1. Refraction at an interface between a transparent object and the air.

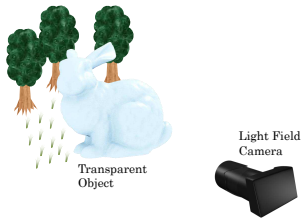

Figure 2. Overview of the proposed method.

Taylor expansion around $\theta_{\text{air}} = \pi/2$ gives us

$$\Psi(\theta_{\text{air}}) \quad = \quad \frac{\frac{\pi}{2} - \theta_{\text{air}}}{\sqrt{n^2 - 1}}, \tag{5}$$

because first and third term are zero. This equation show that $\Psi(\theta_{\text{air}})$ is a monotonic decrease to θ_{air}. The closer θ_{air} get to $\pi/2$, the more $|\Psi(\theta_{\text{air}})|$ is small, and $\Delta\theta_{\text{tra}}$ is also closer to zero. Besides, the higher n, the more $|\Psi(\theta_{\text{air}})|$ is small. In this way, at the boundary contour of transparent object, because $\Delta\theta_{\text{tra}}$ is small with respect to the change of angle of the line of sight, photo-consistency around the boundary contours is maintained. We call the property as local photo consistency. In the proposed method, the boundary contour of the transparent object is estimated by the local photo consistency.

4. Depth Estimation based on Light Field Convergency

The overview of the proposed method is shown in Figure 2. First, a transparent object is captured by a light field camera. The acquired image by light field camera is regarded as the images taken by virtual camera array. Since the spatial intervals between each pair of virtual cameras are short, the convergence angles between the virtual cameras are also small. Next, the corresponding points on the boundary contour are identified from array based on local photo consistency. Then, the depth of the points on the boundary contour from the light field camera is estimated. In addition, the normal direction of surface at the boundary contour and refraction influence are estimated using light field convergency map. The surface shape of the transparent object is updated by minimizing energy function which is composed by the normal direction and refraction influence.

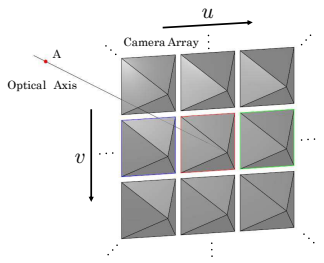

Figure 3. Camera array.

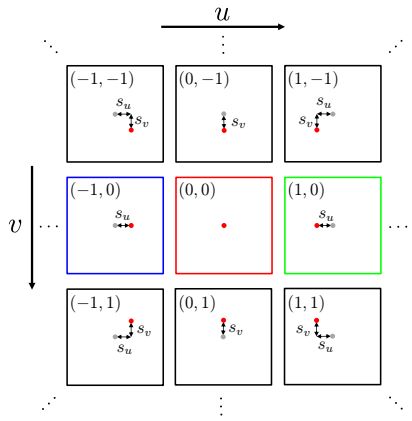

Figure 4. Disparity on camera array images.

4.1. Estimation of Initial Depth

As shown in Figure 3, let us consider that an array of cameras are aligned vertically and horizontally at regular intervals. Array images taken by the camera array to a point A on the optical axis at the camera in the center are shown in Figure 4. The point A is shifted from the center according to the position of the camera. Let s_u be u direction component of the disparity, s_v denotes v direction component of the disparity. The line of sight from the camera is converged one point when s_u and s_v are same value. By changing the disparity s_u and s_v that are same, the line of sight from the camera is converged at an arbitrary depth. Let u and v be the indices corresponding to the position of the camera, $I^{(u,v)}(x,y)$ denotes the acquired image by the camera (u,v), $I_{\text{sh}}^{(u,v)}(x,y,s_u,s_v)$ denotes the image that has moved in parallel an image $I^{(u,v)}(x,y)$ in the direction of returning the shift depending on (u,v) and s_u and s_v, N_{uv} is the total number of camera. In this study, we define the following equation as an error function of the pixel (x,y) expressing

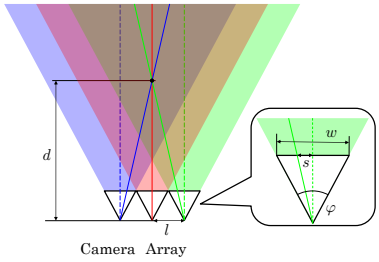

Figure 5. Relationship between parallax and depth.

the light field convergency.

$$E(x, y, s_u, s_v) = \sum_{x',y'} \sum_{u,v} \{I_{\mathrm{sh}}^{(u,v)}(x', y', s_u, s_v) - I_{\mathrm{a}}(x', y', s_u, s_v)\}^2, \quad (6)$$

$$I_{\mathrm{a}}(x, y, s_u, s_v) = \frac{\sum_{u,v} I_{\mathrm{sh}}^{(u,v)}(x, y, s_u, s_v)}{N_{\mathrm{uv}}}. \quad (7)$$

The boundary contour of the transparent object and the background of the corresponding points are searched by obtaining $s = s_u = s_v$ as the error function E is minimized. The parallax image $\hat{s}_0$ is obtained by determining s when the error function E is minimized as follows:

$$\hat{s}_0(x, y) = \arg\min_s E(x, y, s, s). \quad (8)$$

As shown in Figure 5, let us consider a case where three cameras oriented in the same direction look at any one point. Let w be the pixel width of acquired image by the camera, φ is the angle of view of the camera, l is the distance between cameras. Relationship between the disparity s and the depth d is as follows:

$$d = \frac{wl}{2s \tan(\varphi/2)}. \quad (9)$$

Therefore, initial depth d_0 is estimated substituting $\hat{s}_0$ to s in this equation.

4.2. Estimation of Normal Direction

As shown in Figure 6, when looking at the boundary contour which direction of surface is v direction, an image of E with respect to s_u and s_v becomes light field convergency map such as that shown in Figure 7. In this case, as explained in Section 3, even if a viewpoint changes to v direction, color of apparent does not change. Therefore, when the value of s_v corresponds to the correct depth, E is relatively small. Then, E is relatively large when s_v has other value. On the other hand, when a viewpoint changes to u direction, the photo consistency is not maintained, color of apparent changes. Therefore, the difference between E of

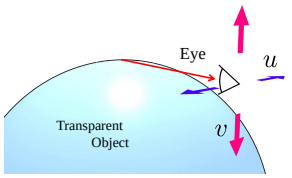

Figure 6. In case of looking at the boundary contour that direction of surface is v direction.

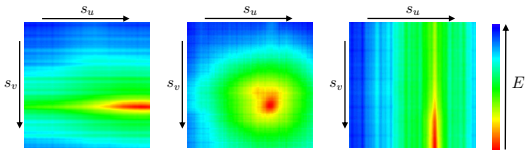

(a) (b) (c)

Figure 7. Light field convergency map. (a): Normal direction of the surface is v direction. (b): Normal direction of the surface is u direction. (c): Normal direction of the surface is slant direction.

when s_u is value corresponding to the correct depth and E at other is relatively small. As a result, as shown in Figure 7 (a), the distribution of the light field convergency map is composed of a long elliptical shape in s_u direction. In contrast, the distribution of the light field convergency map is composed of a long elliptical shape in s_v direction when looking at the boundary contour that faces u direction (Figure 7 (b)). Then, Figure 7 (c) shows the distribution of the light field convergency map when looking at the boundary contour that faces slant direction. Hence, by examining the direction of the elliptical shape of the distribution of the light field convergency map, it is possible to estimate the normal direction of the surface at the boundary contour.

Furthermore, as shown in Figure 8, we consider rotation of disparity. Disparity s_u and s_v are rotated by θ_s, and so s_u and s_v are replaced by s'_u, s'_v and θ_s as follows:

$$s_u = |s'_u \cos\theta_s + s'_v \sin\theta_s|, \quad (10)$$

$$s_v = |s'_v \cos\theta_s - s'_u \sin\theta_s|. \quad (11)$$

Figure 9 shows that light field convergency map depends on θ_s, for example. Let $\hat{\theta}_s$ be angle θ_s of when the ellipticity of the elliptical shape is maximum. We estimate the direction of the surface by the following equation.

$$\theta_{\mathrm{est}} = \begin{cases} \hat{\theta}_s & E''_{u0} \le E''_{v0} \\ \hat{\theta}_s + \dfrac{\pi}{2} & E''_{u0} > E''_{v0} \end{cases}, \quad (12)$$

where $E''_{u0} = \partial^2 E/\partial s_u^2|_{s_u=\hat{s}_0}$ and $E''_{v0} = \partial^2 E/\partial s_v^2|_{s_v=\hat{s}_0}$.

4.3. Estimation of Presence Region of Transparent Object

Figures 10 (a), (b) and (c) show light field convergency maps of when rays converge at a background, a boundary

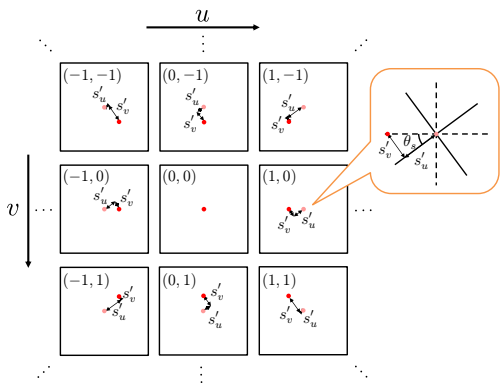

Figure 8. Rotation and shift of point on camera array images.

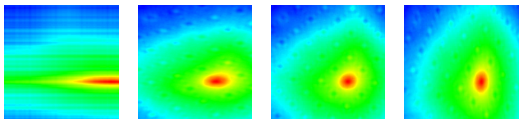

(a) (b) (c) (d)

Figure 9. Angular dependence of light field convergency map. (a): $\theta_s = 0°$. (b): $\theta_s = 30°$. (c): $\theta_s = 45°$. (d): $\theta_s = 60°$.

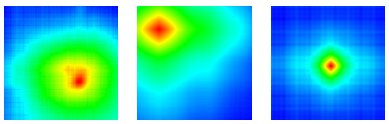

(a) (b) (c)

Figure 10. Influence of refraction to light field convergency map. (a): Boundary contour. (b): Center of sphere shaped transparent object. (c): Background image.

contour and a center of sphere shaped transparent object, respectively. Gradient of distribution of light field convergency map without refraction is steeper than it with refraction. Therefore, we can estimate whether rays were refracted. Let $E_{\min}(x, y)$ be minimum value in light field convergency map. We estimate refraction influence $R(x, y)$ by the following equation as follows:

$$R(x,y) = \frac{\nabla^2_{s_u,s_v} E(x,y,s_u,s_v,0)|_{s_u=\hat{s}_0, s_v=\hat{s}_0}}{E_{\min}(x,y)}, \quad (13)$$

$$\nabla^2_{s_u,s_v} = \frac{\partial^2}{\partial s_u^2} + \frac{\partial^2}{\partial s_v^2}. \quad (14)$$

4.4. Update of Disparity Map

Disparity at points which are not classified as the boundary contour is updated by utilizing an energy function. We define the energy function as follows:

$$E_{s,n}(x,y,s) = k_{\mathrm{A}} F_{\mathrm{ave}}(x,y,s) + k_{\mathrm{B}} F_{\mathrm{g}}(x,y,s) + k_{\mathrm{C}} F_{\mathrm{g0}}(x,y,s), \quad (15)$$

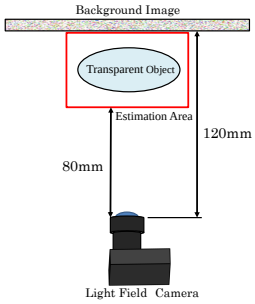

Figure 11. Experimental environment.

where k_{A},k_{B} and k_{C} are coefficients, $F_{\mathrm{ave}}(x, y, s)$ is moving average including weight and $F_{\mathrm{g}}(x, y, s)$ is moving average of gradient including weight, respectively. $F_{\mathrm{g0}}(x, y, s)$ holds gradient at the contour. The more similar θ_{est} and the calculated normal direction from the gradient of $\hat{s}_0$ are, the more influence increases. The contour is obtained by binarizing R and extracting contour. The silhouette is obtained by covering the most outer contour. The weight is set as; 0 at outer of silhouette, $(r_{\max} - r)/r_{\max}$ at others, where r is distance from most outer contour, $r_{\max}$ is maximum value of r. We calculate $\hat{s}_{n+1}$ when $E_{s,n}(x, y, s)$ is minimum as follows:

$$\hat{s}_{n+1}(x,y) = \hat{s}_n(x,y) - \frac{k_s}{\sum_{x,y} E_{s,n}(x,y,s)} \frac{\partial E_{s,n}(x,y,s)}{\partial s}, \quad (16)$$

where k_s is a coefficient for updating. This calculation is applied in silhouette excluding the area around most outer contour. This calculation is iterated until the value of second term is below a threshold.

5. Experimental Results

To confirm that the normal direction of surface and the depth at the boundary contour of the transparent object can be estimated with the proposed method, we conducted experiments with the captured image.

5.1. Simulation

As shown in Figure 11, a light field camera was placed 120 mm from the background plane, the transparent object was placed within the distance of 80 mm to 120 mm from the light field camera. An acquired image by a light field camera is created as a acquired image by a camera array. The array image consists of 6×6 images. Imaginary baseline between cameras is 0.3 mm. Resolution of each array image is 1078×748 pixels. A captured image is made using Blender which is a rendering software. We assume that typical soda-lime glass, the refractive rates of the transparent object is 1.51.

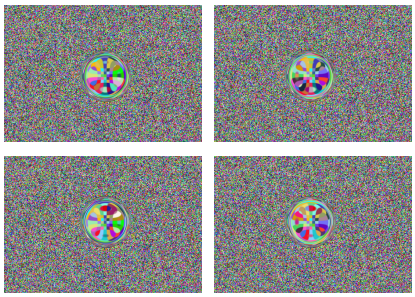

Figure 12. Part of camera array images of Sphere.

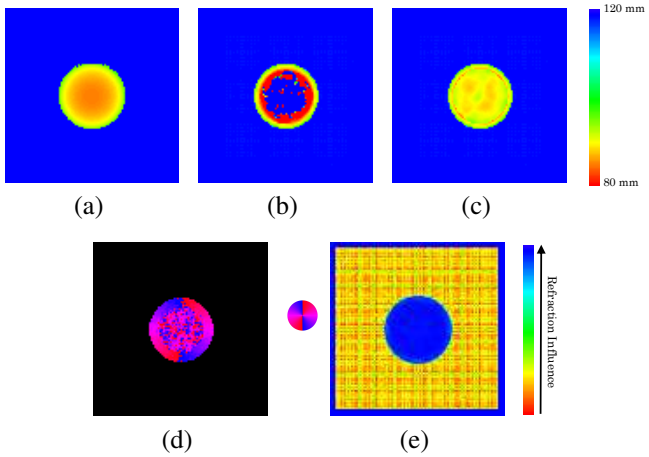

Figure 13. Result of Sphere. (a) Actual depth. (b) Initial depth. (c) Estimated depth. (d) Normal direction. colors show direction of normal. (e) Refraction influence.

Figure 12 shows a part of the acquired array images with Sphere shaped transparent object and Figure 13 shows the estimated depth. Figures 14 - 15, 16 - 17 and 18 - 19 show the case of Torus, Torus-fill and Bunny, respectively. Torus-fill is an object which inside of torus shaped object is filled. Table 1 shows average errors; $\sum |d_{\mathrm{act}} - d_{\mathrm{init}} \mathrm{or} d_{\mathrm{est}}|/N$, where d_{act} is actual depth, d_{init} is initial depth, d_{est} is estimated depth, and N is the number of pixels. Figure 20 shows depth at middle height which is height of center of Sphere.

Table 1. Average error (mm)

Object	init	est
Sphere	1.86	0.456
Torus	0.96	1.51
Torus-fill	5.16	1.06
Bunny	1.33	1.16

5.2. Experiment

To confirm that the normal direction of surface and the depth of the transparent object can be estimated with the proposed method, we conducted experiments with the captured image. As shown in Figure 11, the situation is same as the simulation. Lytro Illum was used as a light field camera. Array image of Lytro Illum consists of 12×12 images, 6×6 images of them are used to estimate. Two types of the transparent object, Apple and Tiger were employed for the experiment.

Figure 21 shows a part of the acquired array images with Apple and Figure 22 shows the estimated depth. Figure 23 shows a part of the acquired array images with Dragon. Figure 24 shows the estimated depth.

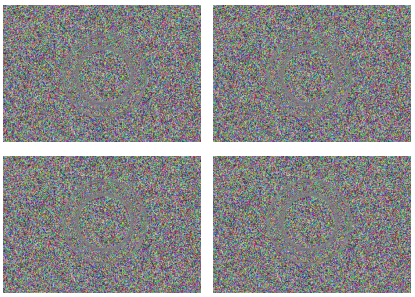

Figure 14. Part of camera array images of Torus.

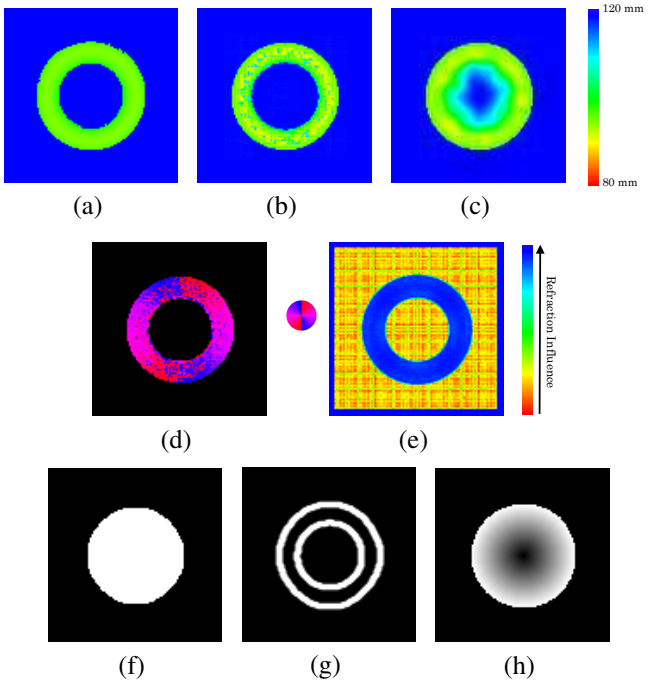

Figure 15. Result of Torus. (a) Actual depth. (b) Initial depth. (c) Estimated depth. (d) Normal direction. (e) Refraction influence. (f) White shows calculation area. (g) White shows contour. (h) Brightness shos weight, white is heavy.

5.3. Discussion

Fig. 13 (b) shows that the depth of only boundary contour have been measured correctly. On the other hand, the depth around the center in Fig. 13 (c) has been improved

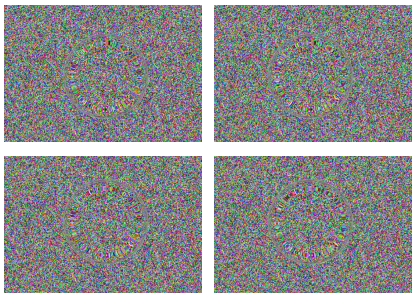

Figure 16. Part of camera array images of Torus-fill.

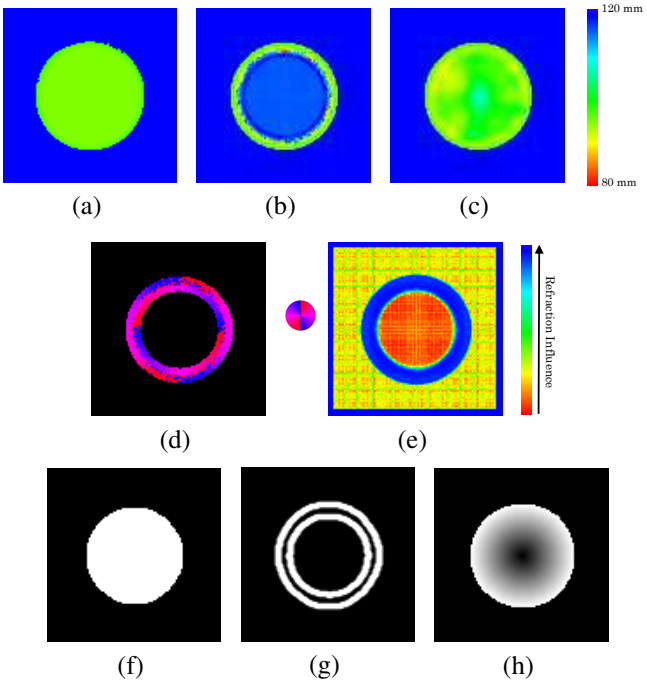

Figure 17. Result of Torus-fill. (a) Actual depth. (b) Initial depth. (c) Estimated depth. (d) Normal direction. (e) Refraction influence. (f) White shows calculation area. (g) White shows contour. (h) Brightness shos weight, white is heavy.

by introducing the update process. Fig. 15 shows that the depth of most of the areas in (b) were almost correctly estimated. The depth in (c) were rather worse than it in (b). In case of Torus, the initial depth were almost correct because most of the areas were regarded as boundary contour. However, because the calculation areas shown in (f) included the area of the inside of Torus, the depth in (c) become little worse. Fig. 17 shows that the depth of boundary contour in (b) were almost correctly estimated, but the depth of around the center in (b) were not estimated. In spite of the fact that (e)〜(h) in Figs. 15 and 17 were similar, the depth of around the center in (c) were improved by updating disparity, like Sphere. F_{g0} effectively worked because (d) in Figs. 15 and 17 are different, that is why this happen. Then, (b) in Figs. 15 and 17 were not able even to be distin-

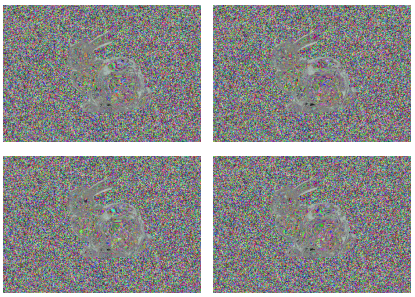

Figure 18. Part of camera array images of Bunny.

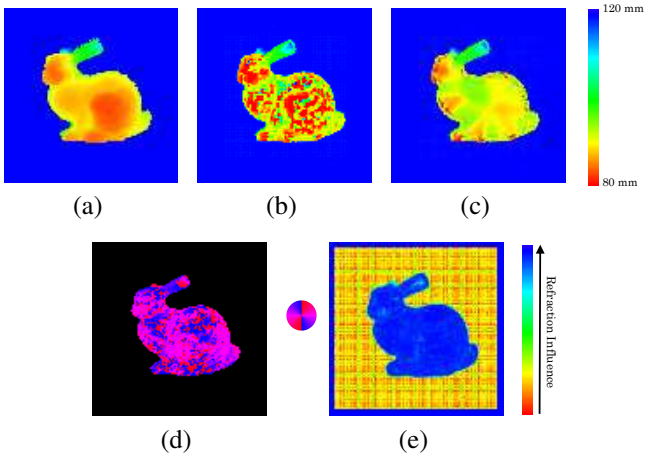

Figure 19. Result of Bunny. (a) Actual depth. (b) Initial depth. (c) Estimated depth. (d) Normal direction. (e) Refraction influence.

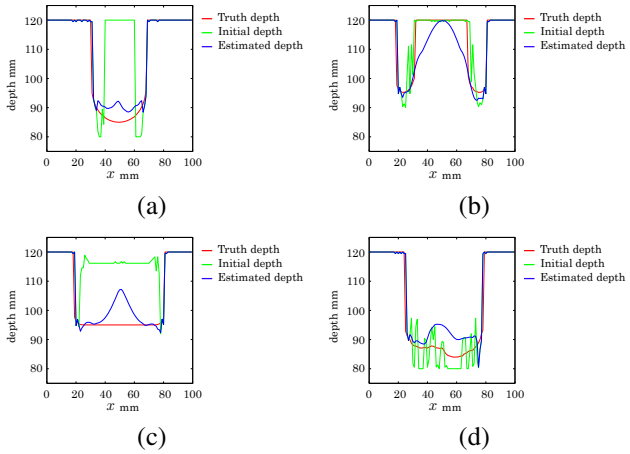

Figure 20. Comparision of depth at middle height. (a): Sphere. (b): Torus. (c): Torus-fill. (d): Bunny.

guished. On the other hand, difference of (c) in Figs. 15 and 17 were obvious. Fig. 19 shows that (c) was initial depth such as correct areas and incorrect areas were mixed. Then, it is seem that the depth in (c) were a little improved by updating disparity. Tab. 1 numerically shows that the depth of

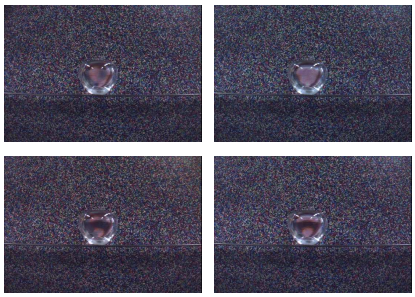

Figure 21. Part of camera array images of Apple.

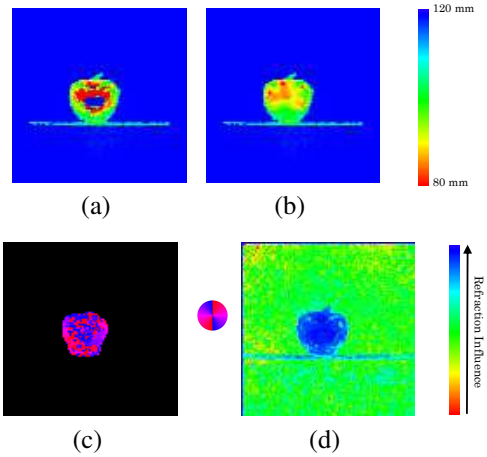

Figure 22. Result of Apple. (a) Initial depth. (b) Estimated depth. (c) Normal direction. (d) Refraction influence.

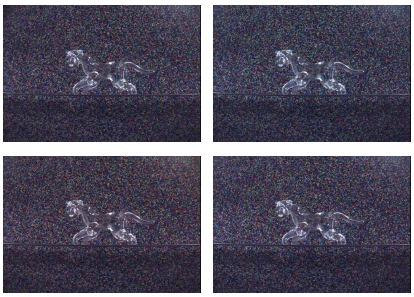

Figure 23. Part of camera array images of Tiger.

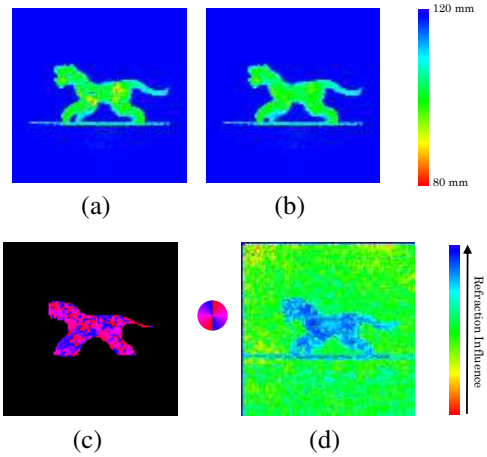

Figure 24. Result of Tiger. (a) Initial depth. (b) Estimated depth. (c) Normal direction. (d) Refraction influence.

overall object were improved by updating disparity, except for result of Torus. From these results, it was confirmed that the depth were almost correctly estimated by the proposed method. Fig. 20 also clearly shows that estimated results excepting (b) were improved by updating disparity. Moreover, it is seen that even initial depth of boundary contour were correctly estimated. From Fig. 22, it is seen that the depth of around the center in (a) were not correct. It is seem that the depth of around the center in (b) were improved by updating disparity. From Fig. 24, it is seem that the depth of some areas in (b) were improved by updating disparity. From these results, it was confirmed that these results behaved in the same way as in case of simulation. Therefore, It was shown that proposed method is practical.

5.4. Limitation

It is needed by the proposed method that the whole of transparent object is captured by light field camera. Proposed method probably cannot estimate shape of transparent object that causes strong specular reflection, because intensity from background became relatively weak. Proposed method usually does not work in case of a background image which passive stereo method causes mismatch. Estimation accuracy depends on the aperture size of a light field camera and the distance from a light field camera to a transparent object. Therefore, estimation accuracy is down when large transparent object is estimated.

6. Conclusion

In this study, we have proposed a method for estimating the surface of transparent object based on light field convergency. In proposed method, a transparent object which is placed in front of a background was captured by the light field camera. The initial depth is estimated using local photo consistency that is occured in a special case of light field convergency. The normal direction and the refraction influence are estimated using light field convergency map which is a distribution of light field convergency. The estimated depth is updated by minimizing energy function which is composed by the normal direction and the refraction influence. In this paper, the results showed that the estimated result were improved by updating disparity. The proposed method can measure the depth around the boundary of the transparent object, which cannot be measured accurately with conventional methods. The proposed method in combination with other complimentary methods may improve the accuracy.

References

[1] Microsoft kinect for xbox one. http://www.xbox.com/en-US/xbox-one/accessories/kinect (reference 2017-05-16). 2

[2] E. H. Adelson and J. Y. A. Wang. Single lens stereo with a plenoptic camera. *IEEE Trans. Pattern Analysis and Machine Intelligence*, 14(2):99–106, 1992. 1

[3] T. E. Bishop and P. Favaro. Plenoptic depth estimation from multiple aliased views. In *Computer Vision Workshops (ICCV Workshops), 2009 IEEE 12th International Conference on*, pages 1622–1629. IEEE, 2009. 2

[4] T. E. Bishop and P. Favaro. Full-resolution depth map estimation from an aliased plenoptic light field. In *Asian Conference on Computer Vision*, pages 186–200. Springer, 2010. 2

[5] C. Chen and Y. F. Zheng. Passive and active stereo vision for smooth surface detection of deformed plates. *IEEE Transactions on Industrial Electronics*, 42(3):300–306, 1995. 1

[6] R. P. Feynman, R. B. Leighton, and M. Sands. *The Feynman Lectures on Physics*, volume 1, chapter 26. Basic Books, 1963. 2

[7] M. B. Hullin, M. Fuchs, I. Ihrke, H.-P. Seidel, and H. P. Lensch. Fluorescent immersion range scanning. *ACM Transactions on Graphics-TOG*, 27(3):87–87, 2008. 1, 2

[8] C. Inoshita, Y. Mukaigawa, Y. Matsushita, and Y. Yagi. Shape from single scattering for translucent objects. In *Proc. European Conf. Computer Vision*, 2012. 2

[9] C. Inoshita, Y. Mukaigawa, Y. Matsushita, and Y. Yagi. Surface normal deconvolution: Photometric stereo for optically thick translucent objects. In *European Conference on Computer Vision*, pages 346–359. Springer, 2014. 2

[10] H. Jin, S. Soatto, and A. J. Yezzi. Multi-view stereo beyond lambert. In *Computer Vision and Pattern Recognition, 2003. Proceedings. 2003 IEEE Computer Society Conference on*, volume 1, pages I–171. IEEE, 2003. 2

[11] K. Koshikawa. A polarimetric approach to shape understanding of glossy objects. In *Proc. International Joint Conf. Artificial Intelligence*, pages 493–495, 1979. 2

[12] K. Maeno, H. Nagahara, A. Shimada, and R. Taniguchi. Light field distortion feature for transparent object recognition. In *Proc. IEEE Conf. Computer Vision and Pattern Recognition*, pages 2786–2793, 2013. 2

[13] D. Miyazaki, M. Kagesawa, and K. Ikeuchi. Transparent surface modeling from a pair of polarization images. *Pattern Analysis and Machine Intelligence, IEEE Transactions on*, 26(1):73–82, 2004. 1, 2

[14] R. Nair, A. Fitzgibbon, D. Kondermann, and C. Rother. Reflection modeling for passive stereo. In *The IEEE International Conference on Computer Vision (ICCV)*, December 2015. 2

[15] R. Ng, M. Levoy, M. Brédif, G. Duval, M. Horowitz, and P. Hanrahan. Light field photography with a hand-held plenoptic camera. *Computer Science Technical Report CSTR*, 2(11):1–11, 2005. 1

[16] M. Saito, Y. Sato, K. Ikeuchi, and H. Kashiwagi. Measurement of surface orientations of transparent objects by use of polarization in highlight. *JOSA A*, 16(9):2286–2293, 1999. 1, 2

[17] J. Salvi, J. Batlle, and E. M. Mouaddib. A robust-coded pattern projection for dynamic 3d scene measurement. *Pattern Recognition*, 19(11):1055–1065, 1998. 1

[18] M. W. Tao, S. Hadap, J. Malik, and R. Ramamoorthi. Depth from combining defocus and correspondence using light-field cameras. In *Proceedings of the IEEE International Conference on Computer Vision*, pages 673–680, 2013. 2

[19] I. Tosic and K. Berkner. Light field scale-depth space transform for dense depth estimation. In *Proceedings of the IEEE Conference on Computer Vision and Pattern Recognition Workshops*, pages 435–442, 2014. 2

[20] S. Wanner and B. Goldluecke. Globally consistent depth labeling of 4d light fields. In *Computer Vision and Pattern Recognition (CVPR), 2012 IEEE Conference on*, pages 41–48. IEEE, 2012. 2

[21] G. Wetzstein, W. Heidrich, and R. Raskar. Computational schlieren photography with light field probes. *International Journal of Computer Vision*, 110(2):113–127, 2014. 1, 2

[22] G. Wetzstein, D. Roodnick, W. Heidrich, and R. Raskar. Refractive shape from light field distortion. In *Proc. IEEE International Conf. Computer Vision*, pages 1180–1186. IEEE, 2011. 1, 2

[23] B. Wilburn, N. Joshi, V. Vaish, E.-V. Talvala, E. Antunez, A. Barth, A. Adams, M. Horowitz, and M. Levoy. High performance imaging using large camera arrays. *ACM Trans. Graphics*, 24(3):765–776, 2005. 1